Raman scattering from magnons, electronic excitations and phonons in antiferromagnetic FeI_2

1994 J. Phys.: Condens. Matter 6 6515

(http://iopscience.iop.org/0953-8984/6/32/013)

J. Phys.: Condens. Matter 6 (1994) 6515–6533. Printed in the UK

Raman scattering from magnons, electronic excitations and phonons in antiferromagnetic FeI_2

D J Lockwood†, G Mischler and A Zwick

Laboratoire de Physique des Solides, associé au CNRS, Université Paul Sabatier, 118 route de Narbonne, 31062 Toulouse Cédex, France

Received 20 December 1993, in final form 26 April 1994

Abstract. The Raman spectrum of FeI_2 has been measured at temperatures above and below the antiferromagnetic ordering temperature $T_N = 9$ K. Spectral features due to Raman scattering from phonons, Fe^{2+}-ion electronic excitations and one- and two-magnon excitations are analysed and assigned. An effective-Hamiltonian model in second order is used to describe the Fe^{2+}-ion levels within the $^5T_{2g}(^5D)$ ground term, and the effects of antiferromagnetic ordering are included in a mean-field model. A comparison is made between the energy-matrix parameters obtained for the related trigonal compounds $FeCl_2$, $FeBr_2$ and FeI_2.

1. Introduction

Raman scattering of light from Fe-group transition-metal ion excitations has now been observed in many compounds (see, for example, the review by Lockwood (1982)). In this family of compounds, light scattering from low-lying electronic and magnetic excitations in the trigonal MX_2 metamagnets (with M=Fe, Co and X=Cl, Br, I) has been the most thoroughly investigated. Currently, the cobaltous dihalides have been extensively studied ($CoCl_2$, Christie and Lockwood 1971a, b, Christie *et al* 1975, Kardontchik *et al* 1977, Lockwood *et al* 1978, 1982; $CoBr_2$, Mischler *et al* 1978, Lockwood *et al* 1979; CoI_2, Mischler *et al* 1987).

For the ferrous dihalides, the first observation of magnons by light scattering as made in $FeCl_2$ (Lockwood *et al* 1978). Detailed results for the temperature dependence of the scattering were reported for $FeCl_2$ by Mischler *et al* (1981) and Lockwood *et al* (1982), and for $FeBr_2$ by Psaltakis *et al* (1984). Electronic excitations above and below the Néel temperature have been analysed and assigned to symmetry species in both $FeCl_2$ and $FeBr_2$ (Johnstone *et al* 1978a, 1980). However, no electronic Raman spectrum of FeI_2 has been published before, essentially because of the experimental difficulties, which will be described later. In order to compare the Fe^{2+}-ion electronic energy levels and the phonons of the different Fe dihalides, we have made a detailed study of the low-lying excitations in FeI_2.

The crystallographic structure of anhydrous FeI_2 is similar to that of $FeBr_2$ and CoI_2. The structure is hexagonal CdI_2 layer-type structure with space group $P\bar{3}m1$ (D^3_{3d}) (Wyckoff 1963). Layers of Fe^{2+} ions lying perpendicular to the crystal c axis are sandwiched between two close-packed layers of I^- ions. The Fe^{2+} ion is surrounded by an almost octahedral arrangement of I^- anions and has $\bar{3}m$ (D_{3d}) site symmetry. All the ferrous

† Permanent address: Institute for Microstructural Sciences, National Research Council, Ottawa, Ontario, K1A 0R6, Canada.

0953-8984/94/326515+19$19.50

halides order antiferromagnetically at low temperature. The magnetic ordering temperature of FeI_2 has been determined by a variety of techniques and has been given variously as $T_N = 10$ K (Bizette *et al* 1957) and 9.3 K (Bertrand *et al* 1974) (magnetic susceptibility measurements), 8.9 K (Brade and Yates 1971) (specific heat measurements), 9.3 K (Fert *et al* 1973) (magnetization measurements) and 8.95 K (Petitgrand *et al* 1980) (neutron scattering measurements).

The magnetic structure of FeI_2 has been studied by neutron diffraction (Gelard *et al* 1974) and was shown to be similar to the spin structure of $MnBr_2$. FeI_2 has an antiferromagnetic structure with magnetic moments aligned along the crystal c axis: two adjacent layers with parallel magnetic moments are succeeded by two layers with magnetic moments in the opposite direction. These layers are parallel to the b axis and make an angle of 73° with the ab plane. The result is a structure in which the layers in the ab plane consist of zig-zag chains of ions with magnetic moments directed parallel within a chain, but antiparallel to adjacent chains. These chains are in the b-axis direction. This magnetic structure has been confirmed with ^{129}I Mössbauer measurements (Friedt *et al* 1976). The behaviour of FeI_2 in a magnetic field has been studied by susceptibility measurements (Bertrand *et al* 1974) and magnetization measurements (Fert *et al* 1973, Wiedenmann *et al* 1988, 1989) and by neutron scattering (Wiedenmann *et al* 1988). Measurements in parallel magnetic fields up to 25 T and below T_N distinguish five magnetic phase transitions with metamagnetic behaviour, indicating six different magnetic phases. The nature of some intermediate phases of this complex phase diagram has also been studied by de Graaf *et al* (1975) and by Calis *et al* (1982) and is characterized by changes in the ratio of spins parallel and antiparallel to the c axis.

The very low-lying magnetic excitations of FeI_2 without and with field have been studied by several methods and have provided some information on the magnon dispersion curves. An infrared Fourier-transform spectroscopy spectrum (Petitgrand and Meyer 1976) exhibits three absorption peaks at $\omega_1 = 21.6$ cm^{-1}, $\omega_2 = 29.2$ cm^{-1} and $\omega_3 = 32.2$ cm^{-1} in zero field that are attributed to zone-centre magnons. The first far-infrared antiferromagnetic resonance (AFMR) experiment in an external field has confirmed the presence of only two of these excitations (ω_2 and ω_3) in zero field (Fert *et al* 1978). A second AFMR experiment has shown the three peaks, but ω_2 and ω_3 were attributed to zone-centre spin waves, while ω_1 has been identified with single-ion two-magnon bound-state excitations (Petitgrand *et al* 1980). This last experiment was in agreement with inelastic neutron-scattering investigations (Petitgrand *et al* 1979): the dispersion curves along the c axis exhibit two branches of spin waves and one branch of two-magnon bound states. The complexity of the FeI_2 behaviour in a magnetic field and also the FeI_2 low-lying excitations can be modelled with either four (Petitgrand and Meyer 1976) or eight (Gelard *et al* 1977) interpenetrating magnetic sublattices. However, it is not possible to deduce the exchange parameters from the spin-wave spectrum with the interpretation of four or eight sublattices (Calis *et al* 1982), because the conditions postulated by Tanaka and Uryû are violated (Uryû and Tanaka 1975, Tanaka and Uryû 1976a, b, 1977). More recently Wiedenmann *et al* (1988) from their neutron-scattering investigation derived five exchange parameters corresponding to three in-plane interactions and two of three inter-plane interactions. Optical spectra have been reported in the 39 000–52 000 cm^{-1} region by Tubbs (1968), in the 4000–16 600 cm^{-1} region by Van Erk (1974) and in the 16 000–250 000 cm^{-1} region by Pollini *et al* (1984).

In this paper, we report on the Raman spectrum of FeI_2 recorded in the 0–1000 cm^{-1} frequency range at low temperatures above and below the Néel temperature. In section 2, we give a group-theoretical analysis. In section 3 we describe the Raman experiments, and in section 4 results and assignments are summarized. In section 5, a comparison of

the phonons in FeI_2 with other ferrous and cobalt halide lattices is discussed. In section 6 an FeI_2 electronic energy-level calculation is presented and a comparison is made with the energy-matrix parameters obtained for ferrous halides. The results obtained are summarized in the final section, section 7.

2. Group-theoretical analysis

A factor-group analysis of the zero-wave-vector lattice vibrations in FeI_2 shows that in point group $\bar{3}m(D_{3d})$ the six optical modes transform as

$$\Gamma_6 = A_{1g} + A_{2u} + E_g + E_u. \tag{2.1}$$

The *gerade* modes are Raman active, with the A_{1g} (or γ_1^+) mode observable in diagonal polarizations (XX), (YY) and (ZZ) and the E_g (or γ_3^+) modes visible in all polarizations except (ZZ).

The diamagnetic surroundings of the ferrous ion in FeI_2 form a slightly distorted octahedron leading to $\bar{3}m$ site symmetry for the ion. The energy-level scheme for a single Fe^{2+} ion in a trigonal site is now well known (see, e.g, Johnstone *et al* 1978a and references therein). The lowest free-ion $^5D(3d^6)$ term is split by the dominant cubic component of the crystal field into a doublet (^5E_g) and a triplet ($^5T_{2g}$). In $FeCl_2$ and $FeBr_2$ the $^5T_{2g}$ orbital triplet lies lowest and the same may be expected for FeI_2. Since the spin–orbit coupling and residual trigonal part of the crystal field are smaller than the cubic field, the $^5T_{2g}$ ground term can be treated as possessing an effective orbital angular momentum $L' = 1$ and spin $S = 2$. The combined effect of these three perturbations is to produce 15 states that may be conveniently grouped into three manifolds characterized by $J' = 1$, 2 and 3 (with $J' = L' + S$) lying near 0, 200 and 500 cm^{-1}, respectively (Johnstone *et al* 1980). The resulting energy-level scheme is given in figure 1, where it should be noted that the order of some levels is sensitive to the trigonal field strength. All levels transform according to either the γ_1^+, γ_2^+ or γ_3^+ representations of the $\bar{3}m$ point group. Selection rules for electronic Raman transitions from the $T^A_{2x\pm}(\gamma_3^+)$ ground and thermally populated $T^A_{2x0}(\gamma_1^+)$ states are given in figure 1.

3. Experiment

The crystal of FeI_2 was grown by the Bridgman method by S Legrand (CEN Saclay). The deep black colour of FeI_2 and its mechanical properties necessitate surface scattering experiments. The samples were prepared in a dry box by cleaving the boule to produce disc-shaped sections approximately 2 mm thick, with the major faces perpendicular to the crystal c axis. The thinner disc-shaped section has a dark red colour. FeI_2 is extremely hygroscopic compared with the other transition-metal dihalides and is more hygroscopic than CoI_2. It was very difficult to obtain shiny cleaved surfaces without the presence of moisture, because the sample surface tarnished in a few seconds in the dry-box atmosphere. Therefore a final thin crystal layer was carefully peeled away just before the Raman measurements. Since the quality of the Raman spectrum is determined by the quality of the surface, care was also taken to produce a surface free of scratches and ripples. Freshly peeled samples were immediately mounted in an Oxford Instruments CF204 cryostat where the sample was immersed in He exchange gas. The sample temperature was monitored with a Scientific

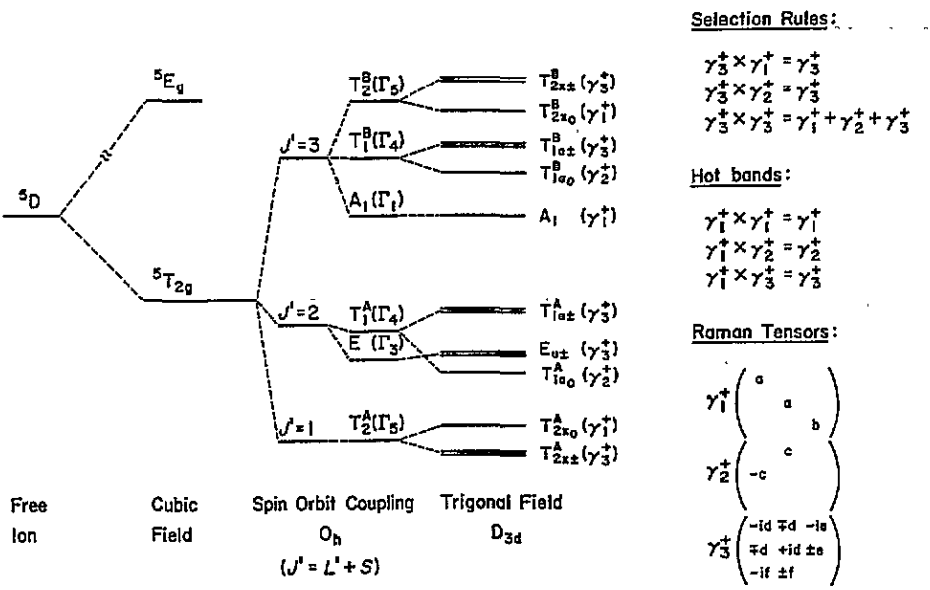

Figure 1. The energy-level scheme for the ground $^5T_{2g}(^5D)$ term appropriate to an Fe^{2+} ion in a trigonal field. Selection rules governing transitions from the $J' = 1$ manifold are given together with the electronic Raman scattering tensors.

Instruments N1G Ge thermometer mounted on the Cu sample block, very close to the crystal surface.

In order to minimize laser heating in the sample and to maximize the scattered light intensity, different exciting wavelengths were tried. Because of the possibility of resonance enhancement, as observed in Raman scattering from Fe^{2+} ions in CdI_2 (Johnstone and Dubicki 1980a, b), and because complete optical absorption measurements in the visible region were not available, we tried 457.9, 465.8, 472.7, 476.5, 488.0, 496.5, 507.7, 514.5 and 638.4 nm laser radiation. The best results were obtained with 472.7 and 476.5 nm radiation and the intensity of the spectrum was just slightly weaker with 488.0 nm radiation. Therefore, the Raman spectrum of FeI_2 was excited with $\sim$ 100 mW of 476.5 nm or $\sim$ 170 mW of 488.0 nm radiation from a Spectra Physics 164 Ar laser. The laser beam, after passing through an Anaspec 300S filter to reject laser fluorescence and plasma emission lines, was focused along the cleaved surface of the sample at grazing incidence. The incident laser polarization was parallel to the crystal surface (PV configuration) or parallel to the crystal c axis (PH configuration). In this second case, the sample temperature was slightly higher, because of an increased absorption of the laser beam, but the Raman signal was stronger. The light scattered through 90° was collected along the crystal c-axis direction and dispersed with a Coderg T800 triple monochromator having a spectral resolution of 2.6 cm^{-1} at 476.5 nm and 2.5 cm^{-1} at 488.0 nm. The Raman signal was detected with a cooled RCA C31034A photomultiplier, and was processed by Ortec photon counting equipment. Each spectrum was recorded automatically in digital form under Digital Minc 11 computer control. No scattered-light polarization measurements were attempted, because of the experimental difficulties involved in exciting and measuring the *extremely weak* Raman signal.

In Raman experiments, local laser heating of the sample commonly occurs, producing temperature gradients, and the temperature given by the Ge thermometer is not an accurate

representation of the true temperature of the crystal surface. In the studies of other transition-metal dihalides, the measured crystal temperatures were corrected for the difference between the known Néel temperature and the apparent ordering temperature, which was determined from the thermometer temperature at which noticeable changes occurred in the bandshapes of electronic lines (Mischler *et al* 1978). In the case of FeI_2 and for all of the Ar laser lines tried, no distinct changes occurred between the base-temperature spectrum (5.6 K on the thermometer) and a spectrum at a higher temperature. This result indicated that even in the case of the base-temperature spectrum the real sample temperature was higher than the Néel temperature ($\sim$ 9 K), proving considerable laser beam absorption and therefore laser heating ($\gtrsim$ 3.5 K) existed under these experimental conditions.

In order to minimize absorption of the beam and in accordance with the optical measurements of Van Erk (1974), we also tried $\sim$ 100 mW of 638.4 nm radiation (spectral resolution, 1.6 cm^{-1}) obtained from an Ar-laser-pumped Spectra Physics 375 Rhodamine 6G dye laser. The thermometer temperature was thereby reduced from 5.6 K to 4.4 K for the base-temperature spectrum. Furthermore, some electronic lines sharpened, grew in intensity, and exhibited line splitting (see section 4). These dramatic changes in the spectrum showed that the real sample temperature was below the Néel temperature. A study of the Raman spectrum of FeI_2 as a function of temperature indicated that the laser heating was now decreased ($\sim$ 2.5 K), consistent with the lower absorption of the crystal for 638.4 nm radiation (Van Erk 1974). At the same time the intensity of the base-temperature spectrum was lowered, indicating a diminished resonance enhancement in agreement with the earlier study of CdI_2:Fe (Johnstone and Dubicki 1980b).

4. Results and assignments

The complete Raman spectrum of FeI_2 has been recorded in the frequency range 0–900 cm^{-1} at various temperatures above and below T_N (4.4–16.2 K thermometer temperature). Representative results, recorded without analysis of the scattered-light polarization, are given in figure 2. The Raman spectrum for frequencies in the very low-frequency region (0–70 cm^{-1}) and below T_N is given in figure 3. Figure 4 shows the temperature dependence of the low-frequency Raman spectrum (50–350 cm^{-1}) of FeI_2 (sample II).

In order to characterize overlapping lines, the spectra were fitted numerically (by means of a least-squares computer procedure) to a number of damped harmonic oscillators of the form

$$I(\omega) = A^2\Gamma\omega/[(\omega^2 - \omega_0^2)^2 + \Gamma^2\omega^2] \tag{4.1}$$

where ω_0, Γ and $A^2/\Gamma\omega_0$ are the oscillator frequency, damping and height respectively. The Bose population factor was neglected. Good fits were obtained with this model and representative results of the curve resolution are shown in figures 5 and 6. The parameters obtained from the fits are summarized in table 1, which gives for each peak the frequency ω_0, the full width at half maximum Γ, the height $h = A^2/\Gamma\omega_0$ and the integrated intensity given by $h\Gamma = A^2/\omega_0$. Table 1 also gives the peak assignments.

4.1. Phonon lines

All the spectra show two relatively strong narrow lines at 70.3 and 118.2 cm^{-1} (4.4 K spectrum of figure 2). The linewidths are resolution limited. Their relatively weak temperature dependences compared with other features in the spectrum of electronic origin together with a comparison with results from Raman measurements of isostructural compounds (see section 5) confirms that these peaks are the two expected first-order phonons of E_g and A_{1g} symmetry.

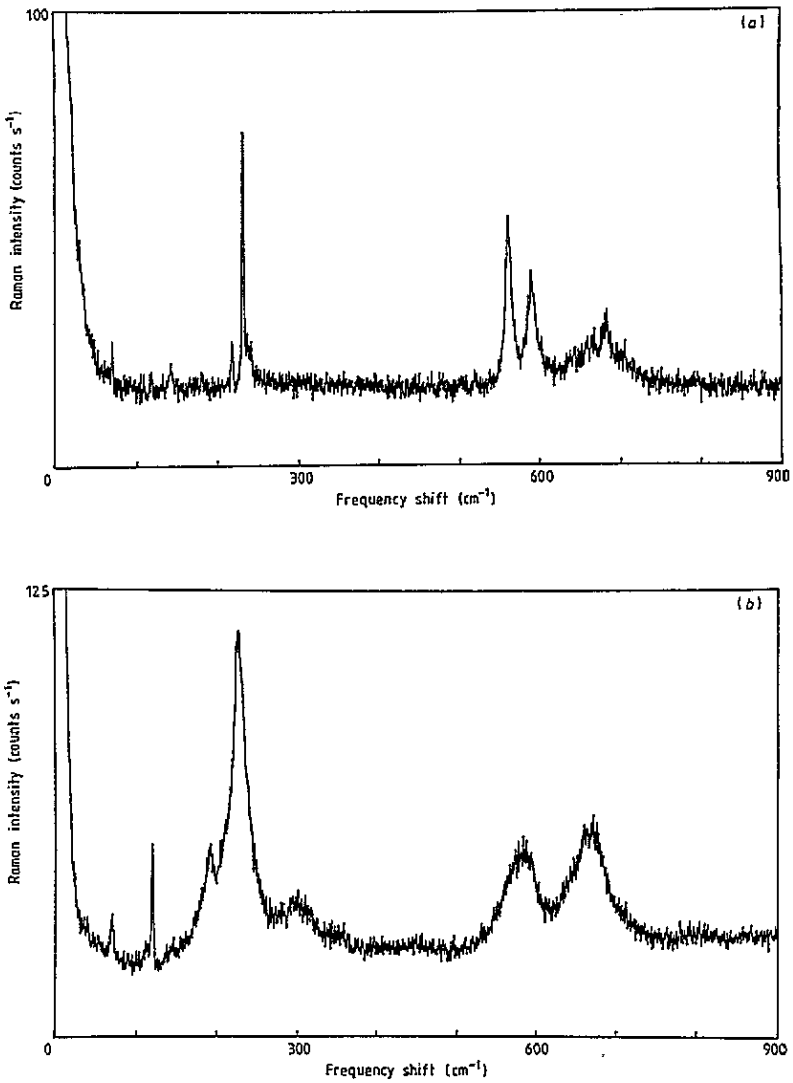

Figure 2. The Raman spectrum of FeI_2 recorded for frequencies between 0 and 900 cm^{-1}: (*a*) sample II at 4.4 K (real temperature < T_N) with the 638.4 nm incident-light polarization parallel to the crystal surface and (*b*) sample III at 5.6 K (real temperature > T_N) with the 476.5 nm incident-light polarization parallel to the crystal *c* axis.

4.2. Electronic lines for $T > T_N$

The nine electronic excitations expected within the $^5T_{2g}$ (^5D) term of Fe^2 ions in paramagnetic FeI_2 must be found amongst the other peaks of table 1.

The high-frequency lines (at 559, 584, 645, 668 and 815 cm^{-1} in the 6.2 K sample I spectra) are necessarily electronic in origin. These bands are very broad ($\Gamma \geqslant 20$ cm^{-1}). When the temperature is increased, only the two more intense bands remain to be fitted (see table 1, sample I). This behaviour of peak intensity decreasing with increasing temperature is typical of electronic Raman bands.

In the 200–500 cm^{-1} region, the 228 and 300 cm^{-1} lines (sample I) exhibit the same

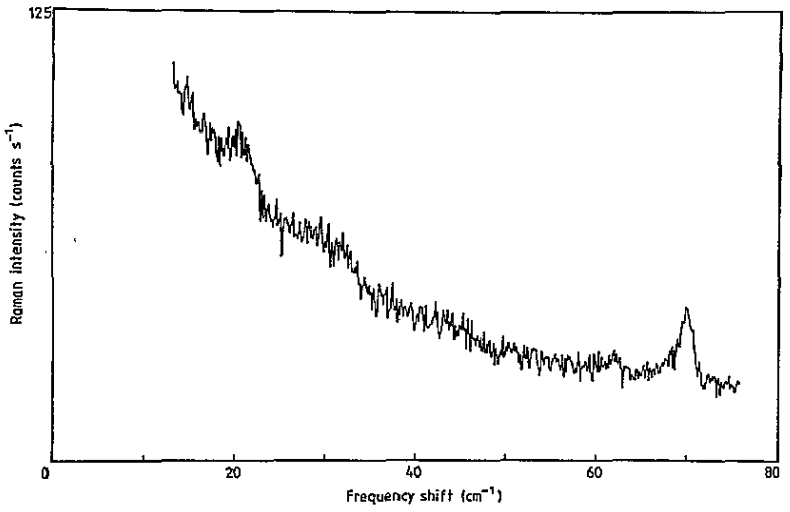

Figure 3. The very low-frequency Raman spectrum of FeI_2 (sample II) at 4.75 K. The 638.4 nm incident-light polarization is parallel to the crystal c axis.

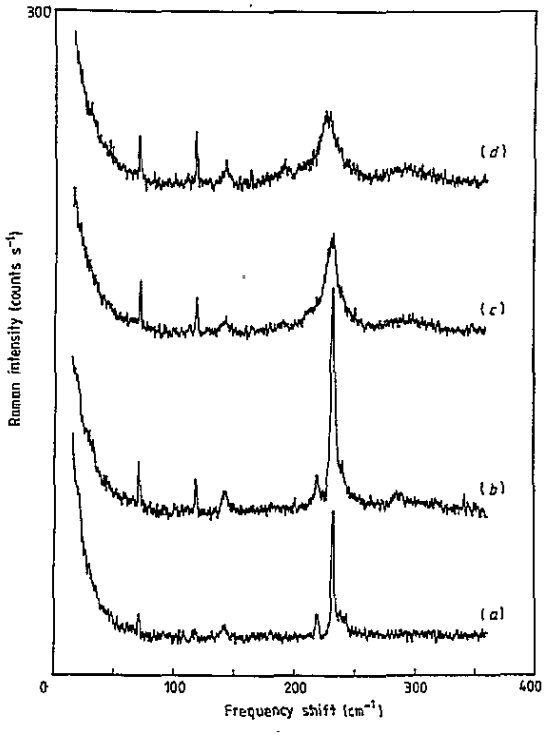

Figure 4. The temperature dependence of the low-frequency Raman spectrum of FeI_2 (sample II) at (*a*) 4.4 K in PV configuration, (*b*) 5.5 K in PH configuration, (*c*) 6.6 K in PH configuration and (*d*) 12.3 K in PH configuration excited with 638.4 nm light (see also table 1).

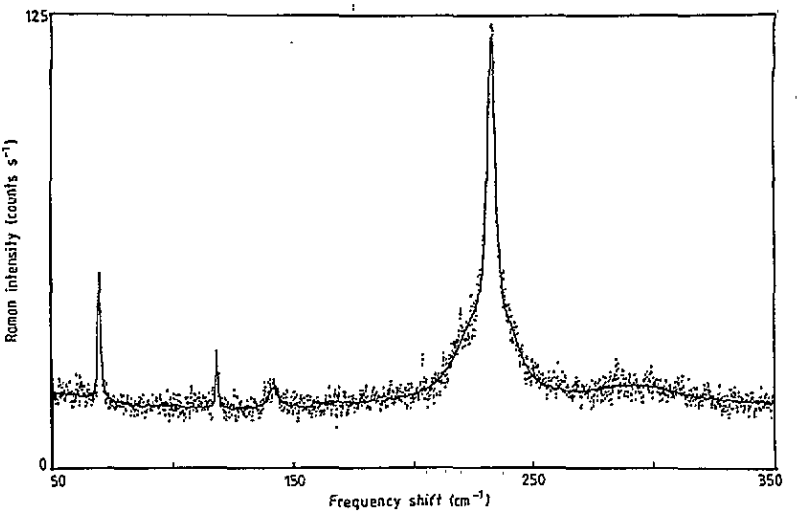

Figure 5. A band fit (full curve) to the 4.4 K Raman spectrum of antiferromagnetic FeI_2 (sample II) in the 50–350 cm^{-1} region (see also table 1).

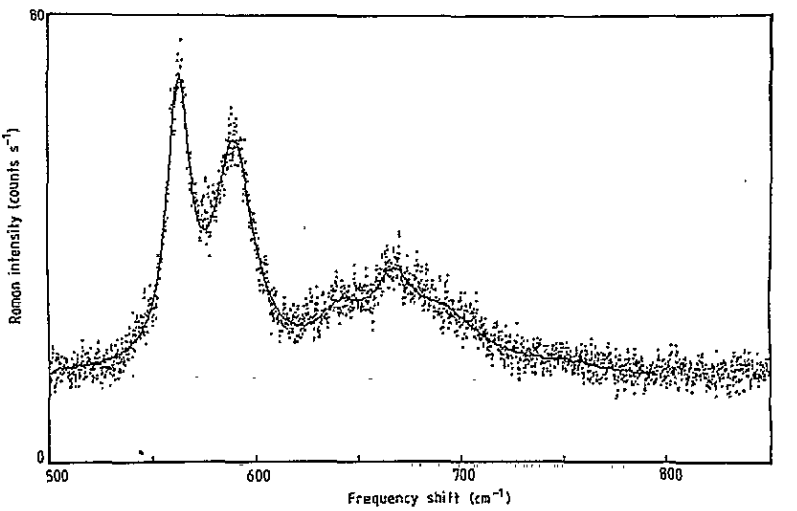

Figure 6. A band fit (full curve) to the 4.4 K Raman spectrum of antiferromagnetic FeI_2 (sample II) in the 500–800 cm^{-1} region (see also table 1).

temperature-dependent behaviour as the high-frequency lines. Of the other lines listed in table 1, only the 210 cm^{-1} line (sample I) is visible in all samples and may be assigned to an electronic excitation, mainly as a consequence of the discussion and assignments concerning the other Raman bands. Finally, the lowest electronic line is not visible in these spectra, because its frequency is too small. For example, it occurs at 8 cm^{-1} in the case of Fe^{2+} ions in CdI_2 (Johnstone and Dubicki 1980a). Further confirmation of the electronic line assignments comes from the energy-level calculation and from comparisons with results for other ferrous halides (see section 6).

4.3. Exciton lines for $T < T_N$

The FeI_2 Raman spectrum changes substantially when the sample is cooled below T_N. The electronic lines sharpen and grow in height, but show only small shifts in frequency (see figures 2 and 4). At lower temperatures, band splittings become apparent. For example, the ~ 580 cm^{-1} band is seen to comprise two separate peaks when the temperature is lowered, as can be seen in figure 2. In figure 4, the 220 cm^{-1} line is clearly separated from the 230 cm^{-1} line when the temperature is decreased. This result indicates clearly that the sample temperature is below T_N (see also section 3). In table 1, we note for each spectrum whether the temperature was below or above T_N.

Below T_N, the 650 cm^{-1} band structure is more complex. Peak frequencies for prominent lines are given in table 1. Although the spectra recorded at 4.4 and 5.1 K (sample II results in table 1) resemble each other (see figures 2 and 6), some differences in the curve-fitting results can be seen. The frequencies of the two most intense peaks (561 ± 1 and 590 ± 1 cm^{-1}) remain much the same, whereas the other three peaks shift down in frequency by 10–20 cm^{-1} with increasing temperature. This indicates a greater sensitivity of the latter three peaks to the exchange interaction, which will be reduced by the increase in temperature for temperatures near T_N. The band at 753 cm^{-1} is certainly only an artifact from the fitting procedure, being required to fill in the base line at higher frequencies to the 650 cm^{-1} group of bands.

Finally, the line at ~ 810 cm^{-1} observed for temperatures above T_N was not visible in the FeI_2 spectra below T_N, which may be due to the fact that the Raman signal was generally weaker with 638.4 nm excitation.

4.4. Magnon lines

In the FeI_2 Raman spectrum, several new features appeared in the very low-frequency region when the crystal was cooled below T_N (see figure 3). One very weak line is visible near 20 cm^{-1} and two very weak overlapping lines appear near 30 cm^{-1}. These three lines are assigned to Raman scattering from magnons. Our Raman observations are thus in general agreement with the AFMR experimental results of Petitgrand and Meyer (1976) who found antiferromagnetic lines at 21.6, 29.2 and 32.2 cm^{-1}. At higher frequencies, there is another weak line at 62 cm^{-1} (close to the E_g phonon of 70 cm^{-1}—see figure 3) that is also associated with magnetic ordering. We tentatively assign this line to two-magnon scattering from the magnon branches near 30 cm^{-1}. It is unlikely to be due to excitons arising from the $T^A_{2x\pm}(\gamma_3^+) \rightarrow T^A_{2x0}(\gamma_1^+)$ transition as its frequency is too high. Because the peaks were very weak and because of the experimental difficulties in studying FeI_2, it was not possible to investigate the temperature dependence of the very low-frequency Raman spectrum of antiferromagnetic FeI_2.

4.5. Other Raman bands

As can be seen in table 1 other Raman bands were found in the FeI_2 spectra.

A weak band at 142.3 ± 1.0 cm^{-1} was visible in all samples. This band is much sharper ($\Gamma \sim 5$ cm^{-1}) than the Fe^{2+} electronic lines and is therefore assigned to two-phonon scattering from the E_g phonon branch. The zone-centre combination frequency is $2 \times 70.3 = 140.6$ cm^{-1}, which is in close agreement with the experimental peak frequency, but combination scattering from other phonons with non-zero wave vectors might also be responsible.

Another weak band at 189.2 ± 0.3 cm^{-1} was also present in all samples. This band is sharper and more intense in samples I and III than in sample II where the band is

Table 1. Parameters obtained from fits to the Raman spectra of antiferromagnetic ($T < T_N$) and paramagnetic ($T > T_N$) FeI_2 recorded at various temperatures: ω_0 (cm^{-1}), peak frequency; Γ (cm^{-1}), full width at half maximum; h (counts s^{-1}), peak height; $h\Gamma$ (arbitrary units), integrated intensity. The laser power, wavelength and spectrometer resolution were for sample I, 170 mW, 488.0 nm and 2.5 cm^{-1}, respectively; for sample II, 100 mW, 638.4 nm and 1.6 cm^{-1}; and for sample III, 100 mW, 476.5 nm and 2.6 cm^{-1}. The incident laser polarization was parallel to the crystal surface (PV configuration) or parallel to the crystal c axis (PH configuration). The temperature given is the temperature of the sample holder and not the actual temperature of the sample surface at the laser beam position.

Sample II 4.4 K ($T < T_N$) PV configuration				Sample II 5.1 K ($T < T_N$) PH configuration				Sample II 5.5 K ($T < T_N$) PV configuration				Sample II 5.5 K ($T < T_N$) PH configuration				Sample II 6.6 K ($T < T_N$) PV configuration				Sample II 6.6 K ($T > T_N$) PH configuration				Sample II 7.8 K ($T > T_N$) PV configuration			
ω_0	Γ	h	$h\Gamma$	ω_0	Γ	h	$h\Gamma$	ω_0	Γ	h	$h\Gamma$	ω_0	Γ	h	$h\Gamma$	ω_0	Γ	h	$h\Gamma$	ω_0	Γ	h	$h\Gamma$	ω_0	Γ	h	$h\Gamma$
70.3	1.1	9.0	10	70.2	1.3	35.2	46	70.2	0.9	11.1	10	70.2	1.1	23.0	25	70.7	0.8	10.3	8	71.1	1.1	23.2	26	70.5	1.5	8.5	13
—	—	—	—	—	—	—	—	—	—	—	—	—	—	—	—	—	—	—	—	—	—	—	—	—	—	—	—
118.2	1.3	4.2	5	118.0	1.0	15.0	15	118.6	1.1	9.3	10	118.4	1.4	17.1	24	118.7	1.8	7.0	13	119.0	1.3	17.6	23	117.7	1.4	3.7	5
142.1	5.4	4.9	26	141.7	4.7	5.7	27	141.7	3.7	11.2	41	142.3	4.0	9.2	37	141.8	2.8	6.5	18	142.6	5.9	6.0	35	142.4	4.4	6.1	27
—	—	—	—	—	—	—	—	—	—	—	—	184.3	39.0	1.5	59	189.6	19.7	2.2	43	184.5	53.8	2.3	124	179.8	40.7	0.7	28
219.2	2.2	10.2	22	224.3	19.7	17.0	335	218.0	2.5	11.0	28	218.2	3.2	12.4	40	218.8	2.7	6.9	19	220.1	26.6	7.3	194	222.3	16.5	3.3	54
231.7	2.3	59.7	137	232.4	4.3	87.6	377	231.6	2.7	39.8	107	231.6	3.7	98.5	364	231.9	3.9	28.7	112	230.4	10.6	36.3	385	229.7	10.3	10.3	106
240.0	8.0	7.4	59	240.7	11.9	11.4	136	240.1	5.2	6.6	34	239.6	9.2	12.4	114	241.1	8.9	5.1	45	240.9	20.8	4.7	98	238.7	7.0	3.9	27
286.5	85.4	1.2	102	293.5	50.0	5.3	265	—	—	—	—	290.5	52.4	5.1	267	280.0	33.0	1.2	40	294.9	40.7	5.6	228	289.6	30.6	2.1	64
—	—	—	—	—	—	—	—	—	—	—	—	—	—	—	—	—	—	—	—	—	—	—	—	—	—	—	—
—	—	—	—	—	—	—	—	—	—	—	—	—	—	—	—	—	—	—	—	—	—	—	—	—	—	—	—
—	—	—	—	—	—	—	—	—	—	—	—	—	—	—	—	—	—	—	—	—	—	—	—	—	—	—	—
560.9	8.4	35.1	295	562.3	12.8	47.1	603	—	—	—	—	—	—	—	—	—	—	—	—	—	—	—	—	—	—	—	—
590.1	14.2	20.1	285	588.8	23.0	38.6	888	—	—	—	—	—	—	—	—	—	—	—	—	—	—	—	—	—	—	—	—
—	—	—	—	—	—	—	—	—	—	—	—	—	—	—	—	—	—	—	—	—	—	—	—	—	—	—	—
659.3	46.8	7.1	332	640.8	29.4	8.2	241	—	—	—	—	—	—	—	—	—	—	—	—	—	—	—	—	—	—	—	—
—	—	—	—	—	—	—	—	—	—	—	—	—	—	—	—	—	—	—	—	—	—	—	—	—	—	—	—
682.3	11.5	8.6	99	666.0	23.2	12.0	278	—	—	—	—	—	—	—	—	—	—	—	—	—	—	—	—	—	—	—	—
703.1	34.3	3.8	130	691.0	48.3	9.9	478	—	—	—	—	—	—	—	—	—	—	—	—	—	—	—	—	—	—	—	—
—	—	—	—	753.0	59.4	1.8	107	—	—	—	—	—	—	—	—	—	—	—	—	—	—	—	—	—	—	—	—
—	—	—	—	—	—	—	—	—	—	—	—	—	—	—	—	—	—	—	—	—	—	—	—	—	—	—	—

Table 1. Continued.

Sample II 12.3 K ($T > T_N$) PH configuration				Sample III 5.6 K ($T > T_N$) PH configuration				Sample I 6.2 K ($T > T_N$) PH configuration				Sample I 16.2 K ($T > T_N$) PH configuration				
ω_0	Γ	h	$h\Gamma$	ω_0	Γ	h	$h\Gamma$	ω_0	Γ	h	$h\Gamma$	ω_0	Γ	h	$h\Gamma$	Assignment
70.4	1.1	20.3	22	70.3	3.0	10.4	31	70.3	2.6	9.0	23	69.6	5.3	9.8	52	E_g one-phonon
—	—	—	—	111.3	5.5	4.7	26	111.9	5.1	4.5	23	112.9	7.6	4.2	32	acoustic phonon combination?
118.4	1.1	25.1	28	119.1	2.3	36.2	83	119.2	2.7	27.6	75	118.7	3.6	23.5	85	A_{1g} one phonon
142.4	3.1	8.2	25	143.3	16.4	3.2	52	141.8	11.9	7.7	92	142.8	8.1	11.9	96	$2 \times E_g$ two-phonon
191.9	19.7	4.7	93	189.3	24.9	16.7	416	189.4	8.8	17.5	154	188.9	15.7	26.9	422	$E_g + A_{1g}$ two-phonon
—	—	—	—	216.5	69.2	11.3	782	209.8	75.5	23.2	1752	205.7	67.2	17.0	1142	electronic
227.6	18.8	29.1	547	228.5	21.5	76.7	1649	228.0	18.8	95.8	1801	226.9	23.2	65.1	1510	electronic
—	—	—	—	—	—	—	—	—	—	—	—	—	—	—	—	$2 \times A_{1g}$ two-phonon
293.8	36.9	5.9	218	301.6	60.9	13.4	816	300.4	63.5	18.4	1168	297.0	45.1	15.9	717	electronic
—	—	—	—	354.7	17.0	2.8	48	355.4	14.5	3.3	48	—	—	—	—	unknown
—	—	—	—	—	—	—	—	—	—	—	—	393.4	343	6.4	2195	artifact from the fitting
—	—	—	—	445.8	30.5	1.8	55	433.6	51.8	2.6	135	—	—	—	—	unknown
—	—	—	—	561.7	24.8	7.1	176	559.3	24.4	11.7	285	—	—	—	—	electronic
—	—	—	—	583.7	38.4	24.3	933	583.7	35.9	38.9	1397	579.2	48.1	33.6	1616	electronic
—	—	—	—	640.5	15.4	3.5	54	645.2	19.7	8.3	160	—	—	—	—	electronic
—	—	—	—	—	—	—	—	—	—	—	—	—	—	—	—	exciton
—	—	—	—	668.0	48.1	32.5	1563	668.2	48.3	35.4	1710	664.4	49.9	34.4	1717	electronic
—	—	—	—	—	—	—	—	—	—	—	—	—	—	—	—	exciton
—	—	—	—	—	—	—	—	—	—	—	—	—	—	—	—	exciton
—	—	—	—	—	—	—	—	—	—	—	—	—	—	—	—	artifact from the fitting
—	—	—	—	807.6	59.4	3.1	184	814.9	76.2	3.2	244	—	—	—	—	electronic combination

very weak and has much the same intensity as the background due to photomultiplier noise. Therefore, the peak frequency and linewidth are not reliable parameters in the fits to the spectra of sample II and hence the integrated intensity values are not reliable for this line. The 189 cm^{-1} line is also assigned to two-phonon scattering, but in this case from a combination of E_g plus A_{1g} phonons. The zone-centre combination frequency of $70.3+118.6 = 188.9$ cm^{-1} agrees very well with experiment. The increased band intensity in samples I and III can only be explained by resonance enhancement through coupling to the adjacent 220 and 230 cm^{-1} electronic lines with 488.0 and 476.5 nm excitation. A similar behaviour has been observed in $CoBr_2$ (Lockwood *et al* 1979), with the analogue of the 189 cm^{-1} band occurring at 250 cm^{-1} (E_g plus A_{1g} phonon combination) and the analogue of the 220–230 cm^{-1} band occurring at 268–270 cm^{-1} (electronic lines). A strong coupling between an electronic transition and the E_g optical phonons has also been observed by light scattering in $FeCl_2$ (Johnstone *et al* 1987b). This resonant coupling may also explain the shift of the ~ 220 cm^{-1} electronic line ($T > T_N$) from one sample to another (220 cm^{-1} for sample II, 217 cm^{-1} for sample III, 210 cm^{-1} for sample I), because this resonant coupling perturbs the electronic energy levels and is also strongly temperature dependent for temperatures near T_N.

The last of the optical two-phonon summation bands is due to A_{1g} phonons and can occur near $2 \times 118.6 = 237.2$ cm^{-1}. A weak band with a relatively sharp line shape compared to electronic lines was visible in sample II at 240.2 ± 1.5 cm^{-1}. This line can most likely be assigned to the overtone of the A_{1g} phonon. The 240 cm^{-1} line is clearly visible at low temperatures, becomes a shoulder of the nearby 230 cm^{-1} electronic line, and then finally disappears with increasing temperature because the linewidth of the 230 cm^{-1} electronic line increases dramatically when the temperature is increased from below to above T_N, as can be seen in figure 4. This combination band is not visible in samples I and III, because of the larger linewidth exhibited by the 230 cm^{-1} electronic band when the temperature is above the Néel temperature.

Another unexplained feature is the low-frequency shoulder to the A_{1g} phonon that is most clearly visible in the spectra of samples I and III. This feature seems to be obscured in sample II, because it has the same intensity as the background signal due to photomultiplier noise. Curve resolving this frequency region reveals a sharp ($\Gamma \sim 6$ cm^{-1}) line with a peak frequency of 112 ± 1 cm^{-1} (see table 1). The origin of this band is not clear, but it is tempting to assign the band to acoustic phonon overtone scattering. However, no acoustic phonon dispersion curves for FeI_2 are available to confirm such an assignment.

Finally, two very weak bands were found at 355 and ~ 440 cm^{-1} in two samples. No clear explanation for these bands has been found, but their presence in only some of the samples suggests they may be due to impurities (i.e., the crystal may not be pure, or there was surface contamination of the sample after cleaving). The line at 393 cm^{-1} in sample I has a large spurious linewidth and is only an artifact introduced from the fitting procedure to account for the lineshape of the noisy baseline of the 300–500 cm^{-1} region.

5. Phonons in FeI_2

The A_{1g} and E_g phonons in FeI_2, which have frequencies of 118.6 ± 0.4 cm^{-1} and 70.3 ± 0.4 cm^{-1} at $\sim$ 10 K, have been readily identified in the Raman spectrum from their resolution-limited widths and weak temperature dependences. However, the lack of good polarization data has precluded a symmetry assignment according to the selection rules of section 2. The symmetry assignments can nevertheless be determined from comparisons

with analogous results for other metal dihalides possessing similar crystal structures. In table 2 we compare low-temperature results obtained for the Raman-active phonons in ferrous and cobaltous dihalides. $FeBr_2$, $CoBr_2$ and CoI_2 have the same crystal structure as FeI_2, whereas $FeCl_2$ and $CoCl_2$ possess the $R\bar{3}m$ (D_{3d}^5) $CdCl_2$ structure (Wyckoff 1963). The $CdCl_2$ structure differs from the FeI_2 structure in the close-packing arrangement of the anions, but again two phonon lines of A_{1g} and E_g symmetry are expected. As table 2 indicates, the FeI_2 phonons at 118.6 and 70.3 cm^{-1} have to be assigned to the A_{1g} and E_g modes, respectively. The FeX_2 phonon frequencies for each mode are remarkably similar to the corresponding CoX_2 case for each halogen indicating little difference in the nature of the metal–halogen bonding in the Fe and Co compounds. The Fe and Co halide phonon frequencies are approximately proportional to the inverse of the square root of the halogen mass. Since the normal modes for the Raman-active phonons comprise halogen motions only (Lockwood 1973), this indicates that the nature of the bonding for these modes is also not very sensitive to the halogen species.

Table 2. A comparison of Raman results for phonon frequencies (in cm^{-1}) in MX_2 compounds at low temperature.

Mode	$FeCl_2$[a]	$CoCl_2$[a]	$FeBr_2$[b]	$CoBr_2$[c]	FeI_2	CoI_2[d]
E_g	149[e]	156.8	94.3	98.0	70.3	70.6
A_{1g}	250.5	253.2	158.4	160.8	118.6	120.0

[a] Lockwood *et al* (1982).
[b] Johnstone *et al* (1978a).
[c] Lockwood *et al* (1979).
[d] Mischler *et al* (1987).
[e] Predicted uncoupled frequency (Lockwood *et al* 1982).

6. Electronic and magnetic excitations in FeI_2

The electronic excitations observed by Raman scattering in FeI_2 generally fall into the groupings near 200 and 500 cm^{-1} shown in figure 1. In this section, we compare experiment with theoretical predictions for these excitations within the Fe^{2+}-ion $^5T_{2g}$ ground term at temperatures above and below T_N and make comparisons with results obtained for other similar iron halides.

6.1. Theoretical analysis for $T > T_N$

An effective-Hamiltonian model of the form (Sugano *et al* 1970)

$$H_{\text{eff}}(^5T_{2g}, D_{3d}) = \Delta(L_Z^2 - \tfrac{1}{3}L(L+1) + \lambda' S_Z L_Z + \lambda(S_X L_X + S_Y L_Y) + \kappa(\boldsymbol{S}\cdot\boldsymbol{L})^2 + \rho(S_x^2 L_x^2 + S_y^2 L_y^2 + S_z^2 L_z^2) \tag{6.1}$$

has been used successfully to describe the electronic excitations in paramagnetic $Fe_{1-x}Mn_xCl_2$ (Johnstone *et al* 1980) and in CdI_2:Fe (Johnstone and Dubicki 1980a) and should likewise apply to FeI_2. In equation (6.1), (XYZ) and (xyz) refer to trigonal and cubic axes, respectively, Δ represents the effective trigonal field, λ and λ' are first-order spin–orbit coupling parameters and κ and ρ are second-order spin–orbit coupling parameters.

A detailed discussion of the various terms in equation (6.1) together with the non-vanishing matrix elements of H_{eff} has been given by Johnstone and Dubicki (1980a).

The lack of useful polarization information in the electronic Raman spectra obtained for FeI_2 makes it difficult to assign the $^5T_{2g}$ energy levels on that basis. The electronic Raman spectra of the similar trigonal layered compounds $FeCl_2$ (Johnstone *et al* 1978a, 1980), $FeBr_2$ (Johnstone *et al* 1978a) and CdI_2:Fe (Johnstone and Dubicki 1980a) are, however, well known and comparison with these results greatly facilitated the FeI_2 assignments. For the $J' = 3$ manifold, the Raman lines at 561, 584, 643 and 688 cm^{-1} may be readily assigned to the A_1 T^B_{1a0}, $T^B_{1a\pm}$ and $T^B_{2x\pm}$ energy levels, respectively. The T^B_{2x0} level lies very close to the uppermost $T^B_{2x\pm}$ doublet in $FeCl_2$, $FeBr_2$ and CdI_2:Fe and probably could not be resolved in the FeI_2 case due to the large breadths of the $J' = 3$ Raman lines. This was also the case for $FeCl_2$ (Johnstone *et al* 1978a, 1980). The electronic line at 811 ± 4 cm^{-1} is too high in frequency to belong to the $J' = 3$ manifold and is readily assigned to an electronic combination band of the two strong electronic peaks at 228 and 584 cm^{-1}. For the $J' = 2$ manifold, and by comparison with $FeBr_2$ in particular, the strongest peak at 228 cm^{-1} must be associated with the lowest T^A_{1a0} level, while the weaker broader line at 301 cm^{-1} belongs to the highest $T^A_{1a\pm}$ level. The intermediate $E_{u\pm}$ energy level could not be resolved. From the curve resolving of the spectra in this region, a weaker band lying just below the 228 cm^{-1} line at ~ 213 cm^{-1} was found (see table 1). This line appears to be electronic in origin, but would not be expected to be the missing $E_{u\pm}$ level based on the other Fe halide results.

Using equation (6.1) and the energy level assignments outlined above, the experimental frequencies were least-squares fitted yielding the results and effective Hamiltonian parameters given in table 3. There is excellent agreement between the theoretical and experimental energies and the $J' = 3$ T^B_{2x0} level is predicted to lie just a few wave numbers below the $T^B_{2x\pm}$ level, as expected. The $J' = 2$ $E_{u\pm}$ level is predicted at 239.1 cm^{-1}. Another calculation was performed taking the 213 cm^{-1} line as the missing $E_{u\pm}$ level, but an unreasonable and very poor fit ensued. The $J' = 3$ levels dictate that the T^A_{1a0} singlet must lie lowest in the $J' = 2$ manifold. Although the 213 cm^{-1} line cannot be a member of the $J' = 2$ manifold it is clearly electronic in origin (see, for example, the $T < T_N$ spectra in figures 2, 4 and 5). It may possibly be a hot band associated with the quite intense 228 cm^{-1} line. Such a hot band associated, in that case, with the lowest member of the $J' = 3$ manifold was observed previously for $FeCl_2$ and $FeBr_2$ (Johnstone *et al* 1978a). If this is the case in FeI_2 the lowest-lying $J' = 1$ T^A_{2x0} level is thus predicted to lie at approximately $228 - 213 = 15$ cm^{-1}, which is very close to the predicted value of 19.6 cm^{-1} (see table 3). Thus it is very likely that the 213 cm^{-1} line is a hot band.

Table 3 also shows the results of fits of equation (6.1) to electronic Raman spectra for $FeCl_2$, $FeBr_2$ and CdI_2:Fe. The earlier results for $FeCl_2$ (Johnstone *et al* 1980) and CdI_2:Fe (Johnstone and Dubicki 1980a) are essentially reproduced here, but this is the first time that the $FeBr_2$ data has been treated with an effective-Hamiltonian model. The order of the energy levels in $FeBr_2$ is well reproduced by the model, but the energy levels are not as accurately predicted as in the other compounds no matter how the energy-level assignments were rearranged (within reason). The disagreement was most evident for the $J' = 1$ and $J' = 2$ manifolds, whereas the $J' = 3$ levels fitted reasonably well. It may be that the dynamic Jahn–Teller mechanism invoked originally (Johnstone *et al* 1978a) to explain the $FeCl_2$ and $FeBr_2$ energy levels is still required to fully account for these variations. Nevertheless, the results are good enough for comparisons to be made.

All the chemical compounds in table 3 possess the hexagonal CdI_2 crystal structure except for $FeCl_2$, which has the related $CdCl_2$ structure (Wyckoff 1963) of space group

Table 3. Calculated and observed energies of the $^5T_{2g}(^5D)$ ground term of ferrous halides. All energies and matrix parameters are in cm^{-1} units.

	$FeCl_2$		$FeBr_2$		FeI_2		CdI_2:Fe	
	Experiment[a,b]	Calculation	Experiment[a]	Calculation	Experiment	Calculation	Experiment[c]	Calculation
Electronic state								
$T^A_{2x\pm}(\gamma_3^+)$	—	0	—	0	—	0	—	0
$T^A_{2x0}(\gamma_1^+)$	28 ± 3	31.6	23 ± 3	44.3	15 ± 5	19.6	8 ± 3	4.5
$T^A_{1a0}(\gamma_2^+)$	141 ± 3	143.2	192 ± 1	200.3	228 ± 1	228.0	184 ± 2	181.8
$E_{u\pm}(\gamma_3^+)$	—	149.0	244 ± 1	225.3	—	239.1	171 ± 1	171.7
$T^A_{1a\pm}(\gamma_3^+)$	216 ± 2	215.3	296 ± 1	304.6	301 ± 1	301.0	202 ± 2	201.3
$A_1(\gamma_1^+)$	462 ± 2	461.8	517 ± 1	517.4	561 ± 2	560.1	522 ± 1	520.4
$T^B_{1a0}(\gamma_2^+)$	—	551.0	—	583.3	584 ± 1	584.2	553 ± 2	558.4
$T^B_{1a\pm}(\gamma_3^+)$	568 ± 3	570.2	584 ± 1	590.7	643 ± 3	644.9	574 ± 1	576.6
$T^B_{2x0}(\gamma_1^+)$	—	620.8	630 ± 1	630.1	—	661.0	600 ± 3	603.1
$T^B_{2x\pm}(\gamma_3^+)$	629 ± 2	628.4	637 ± 1	635.7	668 ± 1	667.7	609 ± 1	606.4
Parameters for energy matrix								
λ		−121.9		−128.3		−119.6		−117.8
λ'		−104.1		−93.5		−114.3		−117.6
κ		−7.97		−12.6		−10.8		−1.76
ρ		45.4		32.4		23.5		23.0
Δ		−96.2		−110.3		−126.1		−35.9

[a] Johnstone *et al* (1978a).
[b] Johnstone *et al* (1980).
[c] Johnstone and Dubicki (1980a).

$R\bar{3}m$ (D_{3d}^5). In all cases the cation site symmetry is $\bar{3}m$ (D_{3d}) and the Fe^{2+} ion is surrounded by a nearly octahedral arrangement of anions. For most compounds, the values obtained for λ and λ' are satisfactorily close to the Fe^{2+} free-ion value of -114 cm^{-1}. The notable exception is $FeBr_2$ (see table 3), which again suggests a discrepancy in the model. For FeX_2 compounds, the anisotropy $\lambda - \lambda'$ in the first-order spin–orbit coupling is quite evident and is consistent with the trigonal distortion of the anion octahedron. The sudden increase in $\lambda - \lambda'$ in going from $FeCl_2$ to $FeBr_2$ may simply be the result of the change in crystal structure. Generally, $\lambda - \lambda'$ decreases going across table 3, consistent with the increasing anion radius, and is essentially zero for CdI_2:Fe, where the trigonal distortion is smallest (Wyckoff 1963). Of the second-order spin–orbit coupling parameters, ρ decreases in magnitude while κ hardly changes in the sequence $FeCl_2 \rightarrow FeBr_2 \rightarrow FeI_2$ just as was found for the equivalent effective-Hamiltonian parameters for the $^4T_{1g}$ (^4F) ground term of Co^{2+} ions in the corresponding Co compounds (Mischler *et al* 1987). In contrast with the Co halides, the effective trigonal field parameter Δ does not show a marked decrease with the sequence Cl $\rightarrow$ Br $\rightarrow$ I, as would be expected, and even exhibits a slight increase. Overall, Δ is much smaller in the Fe compounds than in the Co compounds and the small differences seen here between the different Fe compounds may result from the model fits and thus not be significant. Δ does drop sharply for CdI_2:Fe, which is consistent with the large $\lambda - \lambda'$ anisotropy reduction. The trends seen with the change in halide for the Fe compounds are thus not as clear cut as for the corresponding Co compounds, which could in part be due to the change in crystal structure (from $CdCl_2$ to CdI_2 type) but might also point to limitations in the effective-Hamiltonian model.

6.2. *Theoretical analysis for $T < T_N$*

Below T_N, FeI_2 becomes anitferromagnetic and the single-ion transitions show splittings and shifts due to the formation of excitons consequent upon the long-range order. As the multisublattice magnetic structure of FeI_2 is complicated, the exchange interactions are treated only approximately within the mean-field approximation by adding

$$H_{MF} = \tfrac{2}{3}(J_1 - J_2)S_Z \tag{6.2}$$

to equation (6.1), as was done previously for $FeCl_2$ and $FeBr_2$ (Johnstone *et al* 1978a). In equation (6.2), J_1 and J_2 refer to the dominant intralayer ferromagnetic and interlayer antiferromagnetic exchange parameters, respectively. The mean-field model is expected to be adequate for describing the higher-energy excitons where the dispersion is small, but cannot properly account for lower energy levels, and, in particular, the magnons, where spin correlation effects are important.

For $T < T_N$, only two sharp peaks are visible in the 200 cm^{-1} region of the Raman spectrum (see figure 2). The strongest line at 232 cm^{-1} undoubtedly arises from the equally strong single-ion 228 cm^{-1} transition and the weaker line at 219 cm^{-1} is derived from the single-ion hot band at 213 cm^{-1}. A weak band near 290 cm^{-1} seen only in the strongest spectra (see figure 5 and table 1) probably arises from the similarly weak 301 cm^{-1} single-ion transition. No other magnetic exciton lines in the $J' = 2$ manifold could be found, probably because they are quite weak as in $FeCl_2$ and $FeBr_2$ (Johnstone *et al* 1978a). Five peaks were seen in the $J' = 3$ manifold for $T < T_N$ (see figure 6 and table 1) arising from the strongest single-ion transitions at 561 (singlet), 584 (singlet), 643 (doublet expected, but only one peak was curve resolved) and 668 (doublet) cm^{-1}, respectively. The exciton frequencies measured at the lowest temperature (4.4 K, sample II) were least-squares fitted by varying the exchange parameter $J = J_1 - J_2$ in equation (6.2) while retaining the parameters obtained

from the single-ion fit in equation (6.1). For $J = 9.0$ cm^{-1} the predicted energy levels are in good overall agreement with experiment, as can be seen in table 4. There is some discrepancy for the lowest exciton, as was expected. The excitation at 13 cm^{-1} deduced from the hot band at 219 cm^{-1} does not match the known zone-centre magnon energies in FeI_2 (see section 1) and thus is of unknown origin. It could arise from a lower-lying magnon branch in such a complicated magnetic structure with up to eight sublattices. The calculation showed that the frequencies of the lines at 659, 682 and 703 cm^{-1} are strongly dependent on J, while the 561 and 590 cm^{-1} lines are not so sensitive. This result is in general agreement with the observed temperature (and hence J) dependence of the spectrum, as discussed in subsection 4.3. The exciton feature observed at 659 cm^{-1} is predicted to comprise two closely spaced, but experimentally unresolved, lines. The exciton predicted at 676 cm^{-1} is most likely weak and not resolveable experimentally from the 678 cm^{-1} exciton. Finally, an exciton is predicted at 302.5 cm^{-1} close to the weak peak observed near 290 cm^{-1}.

Table 4. Experimental and calculated energies (in cm^{-1}) of excitons in the $^5T_{2g}(^5D)$ ground term of antiferromagnetic FeI_2 at ~ 5 K. The mean-field exchange parameter J was 9.0 cm^{-1}.

Experimental energy	Calculated energy
0	0
13 ± 2	28.6
—	33.0
232 ± 1	241.9
—	257.2
—	260.6
~290	302.5
—	313.1
561 ± 1	565.9
590 ± 1	604.8
659 ± 3	654.3
659 ± 3	655.4
—	675.7
682 ± 2	678.4
703 ± 3	691.8

The fitted J value of 9.0 cm^{-1} is similar to values obtained earlier for antiferromagnetic $FeCl_2$ ($J = 18.5$ cm^{-1}) and $FeBr_2$ ($J = 14.5$ cm^{-1}) by Johnstone *et al* (1978a) and compares favourably with values deduced by Petitgrand and Meyer (1976) from AFMR measurements ($J = 13.0$ cm^{-1}), by Fert *et al* (1973) and Bertrand *et al* (1974) from the magnetic susceptibility ($J = 7.0$ and 13.1 cm^{-1}, respectively) and by Wiedenmann *et al* (1988) from neutron-scattering studies ($J = 7.3$ cm^{-1}).

6.3. Magnons

As noted earlier in section 1, AFMR and inelastic neutron-scattering measurements have revealed two zone-centre magnons at 29.2 and 32.2 cm^{-1} and a two-magnon bound state at 21.6 cm^{-1}. It was difficult to probe these excitations in the Raman scattering, because of the laser light scattered by the sample, which produced a high stray-light signal near the laser line, and because of the local laser heating. This heating resulted in the actual measurement temperature being closer to T_N, where the magnons can be expected to broaden and shift to lower frequency. Nevertheless, Raman scattering from magnons was observed. Two

low-frequency peaks were observed near 20 and 30 cm^{-1}, as can be seen in figure 3, that correspond very well to the excitations observed earlier by the other techniques. The sharper peak at 20.2 cm^{-1} is the two-magnon bound state, while the broader peak near 30 cm^{-1} that actually comprises two lines at 29.0 and 31.5 cm^{-1} arises from the two one-magnon branches. The Raman frequencies are slightly lower than the AFMR values, as could be expected from the laser-induced sample heating. No lower-frequency magnon peaks could be detected because of the instrumental stray light. The low-frequency Raman spectrum of figure 3 also shows a weak sharp band at 62 cm^{-1} (beside the 70 cm^{-1} E_g phonon) that is magnetic in origin and could be a two-magnon line. Neutron-scattering measurements of the magnon dispersion along the c axis (Petitgrand *et al* 1979) show the two one-magnon branches to be fairly flat and thus a two-magnon peak could be expected near 60 cm^{-1} arising from the usual zone-boundary scattering mechanism (Cottam and Lockwood 1986). Such two-magnon scattering can be comparable in intensity to the one-magnon scattering (Cottam and Lockwood 1986), as observed here.

7. Conclusions

This Raman scattering study of FeI_2 at low temperatures has revealed features associated with phonons and electronic excitations within the $^5T_{2g}(^5D)$ ground term of Fe^{2+} ions. The electronic excitations in paramagnetic FeI_2 are accurately described within an effective-Hamiltonian model, but comparisons of the energy-matrix parameters found for the related compounds $FeCl_2$, $FeBr_2$ and CdI_2:Fe suggest that the model, although adequate, is not a complete description of the physics involved. It may be that the dynamic Jahn–Teller effect, which must operate in these systems, needs also to be considered. It would be informative also to carry out a complete $3d^6$ configuration calculation for these compounds, but this would be a difficult task as it involves multiple diagonalization of a 210×210 matrix within the least-squares fitting procedure.

Below T_N, Raman features due to magnetic ordering were observed. The higher-frequency excitons could be readily interpreted in terms of a molecular-field theory for the exchange that gave an effective exchange constant of 9.0 cm^{-1}. The analysis showed that there is probably a low-frequency magnon branch in FeI_2 near 13 cm^{-1} at zero wave vector. Raman scattering from one-magnon excitations was observed at 29.0 and 31.5 cm^{-1}, in agreement with earlier studies, together with a line at 20.2 cm^{-1} that is due to a two-magnon bound state. Another magnetic peak was found at 62 cm^{-1}; this is probably due to conventional two-magnon Raman scattering.

References

Bertrand Y, Fert A R and Gelard J 1974 *J. Physique* **35** 385–91
Bizette H, Terrier C and Tsaï B 1957 *C. R. Acad. Sci., Paris* **245** 507–9
Brade R M and Yates B 1971 *J. Phys. C: Solid State Phys.* **4** 876–83
Calis G H M, Swolfs A B M and Trooster J M 1982 Chem. Phys. **64** 273–85
Christie J H, Johnstone I W, Jones G D and Zdansky K 1975 *Phys. Rev.* B **12** 4656–65
Christie J H and Lockwood D J 1971a *Chem. Phys. Lett.* **8** 120–2
—— 1971b *Proc. 2nd Int. Conf. on Light Scattering in Solids (Paris, 1971)* ed M Balkanski (Paris: Flammarion) pp 145–50
Cottam M G and Lockwood D J 1986 *Light Scattering in Magnetic Solids* (New York: Wiley)
de Graaf H and Trooster J M 1975 *Solid State Commun.* **16** 1387–91
Fert A R, Bertrand D, Leotin J and Ousset J C 1978 *Solid State Commun.* **26** 693–6

Fert A R, Gelard J and Carrara P 1973 *Solid State Commun.* **13** 1219–23
Friedt J M, Sanchez J P and Shenoy G K 1976 *J. Chem. Phys.* **65** 5093–102
Gelard J, Fert A R, Bertrand D and Carrara P 1977 *J. Physique* **38** 503–7
Gelard J, Fert A R, Meriel P and Allain Y 1974 *Solid State Commun.* **14** 187–9
Johnstone I W and Dubicki L 1980a *J. Phys. C: Solid State Phys.* **13** 121–30
—— 1980b *Proc. IXth Int. Conf. on Raman Spectrosc.* ed W F Murphy (Amsterdam: North-Holland) pp 152–3
Johnstone I W, Lockwood D J, Bertrand D and Mischler G 1980 *J. Phys. C: Solid State Phys.* **13** 2549–66
Johnstone I W, Lockwood D J and Mischler G 1978a *J. Phys. C: Solid State Phys.* **11** 2147–63
Johnstone I W, Lockwood D J, Mischler G, Fletcher J R and Bates C A 1978b *J. Phys. C: Solid State Phys.* **11** 4425–38
Kardontchik J E, Cohen E and Makovsky J 1977 *Phys. Rev.* B **16** 508–14
Lockwood D J 1973 *J. Opt. Soc. Am.* **63** 374–82
—— 1982 *Light Scattering in Solids III (Springer Topics in Applied Physics 51)* ed M Cardona and G Güntherodt (Heidelberg: Springer) pp 59–92
Lockwood D J, Johnstone I W, Mischler G and Carrara P 1978 *Solid State Commun.* **25** 565–8
Lockwood D J, Mischler G, Johnstone I W and Schmidt M C 1979 *J. Phys. C: Solid State Phys.* **12** 1955–75
Lockwood D J, Mischler G, Zwick A, Johnstone I W, Psaltakis G C, Cottam M G, Legrand S and Leotin J 1982 *J. Phys. C: Solid State Phys.* **15** 2973–92
Mischler G, Bertrand D, Lockwood D J, Cottam M G and Legrand S 1981 *J. Phys. C: Solid State Phys.* **14** 945–60
Mischler G, Lockwood D J and Zwick A 1987 *J. Phys. C: Solid State Phys.* **20** 299–309
Mischler G, Schmidt M C, Lockwood D J and Zwick A 1978 *Solid State Commun.* **27** 1141–6
Petitgrand D, Bruna A and Meyer P 1980 *J. Magn. Magn. Mater.* **15–18** 381–2
Petitgrand D, Hennion B and Escribe C 1979 *J. Magn. Magn. Mater.* **14** 275–6
—— 1980 *J. Physique* **41** L135–8
Petitgrand D and Meyer P 1976 *J. Physique* **37** 1417–22
Pollini I, Thomas J and Lenselink A 1984 *Phys. Rev.* B **30** 2140–8
Psaltakis G C, Mischler G, Lockwood D J, Cottam M G, Zwick A and Legrand S 1984 *J. Phys. C: Solid State Phys.* **17** 1735–52
Sugano S, Tanabe K and Kamimura H 1970 *Multiplets of Transition Metal Ions in Crystals* (New York: Academic)
Tanaka Y and Uryû N 1976a *Prog. Theor. Phys.* **55** 1356–72
—— 1976b *J. Phys. Soc. Japan* **40** 404–10
—— 1977 *J. Phys. Soc. Japan* **43** 1569–76
Tubbs M R 1968 *J. Phys. Chem. Solids* **29** 1191–203
Uryû N and Tanaka Y 1975 *Phys. Lett.* **51A** 451–2
Van Erk W 1974 *Thesis* Rijksuniversiteit Groningen
Wiedenmann A, Regnault L P, Burlet P, Rossat-Mignod J, Koundé O and Billerey D 1988 *J. Magn. Magn. Mater.* **74** 7–21
—— 1989 *Physica* B **156&157** 305–7
Wyckoff R W G 1963 *Crystal Structures* 2nd edn, vol 1 (New York: Wiley–Interscience) pp 266–75